

USmorph: An Updated Framework of Automatic Classification of Galaxy Morphologies and Its Application to Galaxies in the COSMOS Field

JIE SONG ^{1,2} GUANWEN FANG ^{3,*} SHUO BA,⁴ ZESEN LIN ⁵ YIZHOU GU ⁶ CHICHUN ZHOU ⁴ TAO WANG ^{7,8}
CAI-NA HAO ⁹ GUILIN LIU ^{10,2} HONGXIN ZHANG ^{10,2} YAO YAO ^{1,2} AND XU KONG ^{1,2}

¹Deep Space Exploration Laboratory / Department of Astronomy, University of Science and Technology of China, Hefei 230026, People's Republic of China; xkong@ustc.edu.cn

²School of Astronomy and Space Science, University of Science and Technology of China, Hefei 230026, People's Republic of China

³Institute of Astronomy and Astrophysics, Anqing Normal University, Anqing 246133, People's Republic of China; wen@mail.ustc.edu.cn

⁴School of Engineering, Dali University, Dali 671003, People's Republic of China

⁵Department of Physics, The Chinese University of Hong Kong, Shatin, N.T., Hong Kong S.A.R., People's Republic of China

⁶School of Physics and Astronomy, Shanghai Jiao Tong University, 800 Dongchuan Road, Minhang, Shanghai 200240, People's Republic of China

⁷School of Astronomy and Space Science, Nanjing University, Nanjing, Jiangsu 210093, People's Republic of China

⁸Key Laboratory of Modern Astronomy and Astrophysics, Nanjing University, Ministry of Education, Nanjing 210093, People's Republic of China

⁹Tianjin Astrophysics Center, Tianjin Normal University, Tianjin 300387, People's Republic of China

¹⁰Key Laboratory for Research in Galaxies and Cosmology, Department of Astronomy, University of Science and Technology of China, Hefei, Anhui 230026, People's Republic of China

ABSTRACT

Morphological classification conveys abundant information on the formation, evolution, and environment of galaxies. In this work, we refine the two-step galaxy morphological classification framework (USmorph), which employs a combination of unsupervised machine learning (UML) and supervised machine learning (SML) techniques, along with a self-consistent and robust data preprocessing step. The updated method is applied to the galaxies with $I_{\text{mag}} < 25$ at $0.2 < z < 1.2$ in the COSMOS field. Based on their HST/ACS I-band images, we classify them into five distinct morphological types: spherical (SPH, 15,200), early-type disk (ETD, 17,369), late-type disk (LTD, 21,143), irregular disk (IRR, 28,965), and unclassified (UNC, 17,129). In addition, we have conducted both parametric and nonparametric morphological measurements. For galaxies with stellar masses exceeding $10^9 M_{\odot}$, a gradual increase in effective radius from SPHs to IRRs is observed, accompanied by a decrease in the Sérsic index. Nonparametric morphologies reveal distinct distributions of galaxies across the $G_{\text{ini}} - M_{20}$ and $C - A$ parameter spaces for different categories. Moreover, different categories exhibit significant dissimilarity in their G_2 and Ψ distributions. We find morphology to be strongly correlated with redshift and stellar mass. The consistency of these classification results with expected correlations among multiple parameters underscores the validity and reliability of our classification method, rendering it a valuable tool for future studies.

Keywords: Galaxy structure (622), Astrostatistics techniques (1886), Astronomy data analysis (1858)

1. INTRODUCTION

In the realm of observational cosmology, galaxy morphology stands out as one of the most readily accessible properties, intimately intertwined with numerous other physical attributes (such as color, gas content, star formation rate, stellar mass, and environment) of galaxies (e.g., Kauffmann et al. 2004; Omand et al. 2014; Schawinski et al. 2014; Kawinwanichakij et al. 2017; Gu et al. 2018; Lianou et al. 2019). It can offer insights into the evolutionary history and assembly processes of galaxies. For example, as galaxies evolve, their morphological features may transition towards being more bulge-dominated and compact (e.g., Martig et al. 2009;

Dimauro et al. 2022). Consequently, accurately estimating galaxy morphology at each epoch within the universe is of fundamental importance for unraveling the intricate tapestry of galaxy evolution.

Several methods are currently available for characterizing galaxy morphology, with one of the most direct being visual inspection. In a pioneering study, Hubble (1926) systematically analyzed approximately 400 galaxies and categorized them using what is now known as the ‘‘Hubble tuning fork’’ classification. Furthermore, the Galaxy Zoo project engaged the efforts of nearly half a million volunteers, resulting in the morphological classification of over one million galaxies (e.g., Lintott et al. 2011; Simmons et al. 2017; Willett et al. 2017; Walmsley et al. 2021). These citizen science initiatives have significantly expanded our knowledge of galaxy

* GuanWen Fang and Jie Song contributed equally to this work

morphologies. However, this method is characterized by low efficiency, high cost, and inherent subjective bias, which may not be suitable for future large-sky surveys.

Besides visual inspection, galaxy morphological classifications can be also obtained with several features from the raw images. This can be achieved through parametric measurement, which involves modeling the galaxy’s light distribution with an analytic function (e.g., de Vaucouleurs 1948; Sérsic 1963; Freeman 1970), and nonparametric measurement (e.g., Conselice et al. 2000; Conselice 2003; Lotz et al. 2004, 2008; Conselice 2014). Using Principal Component Analysis techniques and based on structural parameters (e.g., C, A, Gini, M_{20} , ellipticity, and Sérsic index), Scarlata et al. (2007) classified approximately 56,000 galaxies in the COSMOS (Cosmic Evolution Survey, Scoville et al. 2007) field into early-type, disk, and irregular galaxies. Similarly, according to the distribution of galaxies in the morphological structural parameter space, Cassata et al. (2007) and Tasca et al. (2009) also obtained the morphological classification results in the COSMOS field. This approach represents the characteristics of galaxies using a few parameters, reducing the complexity of describing galaxy morphology, but it also rejects the rich information hidden beneath all the pixels, which may lead to misclassification in some cases.

In recent years, the rapid advancement of computer technology has enabled the application of machine-learning techniques for galaxy morphological classification. This include feature-based methods (e.g., Sreejith et al. 2018; Huertas-Company et al. 2007; Banerji et al. 2010; Gauci et al. 2010) and image-based methods (e.g., Zhu et al. 2019; Ghosh et al. 2020; Vega-Ferrero et al. 2021). Convolutional Neural Networks (CNNs, Schmidhuber 2015), in particular, have demonstrated their ability to replicate human perception and have been successfully used to determine galaxy morphological types in both the local universe (e.g., SDSS - Sloan Digital Sky Survey, York et al. 2000, DES - Dark Energy Survey, Dark Energy Survey Collaboration et al. 2016) and the high-redshift universe (e.g., CANDELS - Cosmic Assembly Near-infrared Deep Extragalactic Legacy Survey, Grogin et al. 2011) (e.g., Dieleman et al. 2015; Zhu et al. 2019; Ghosh et al. 2020; Vega-Ferrero et al. 2021; Cavanagh et al. 2021). However, as an SML method, CNNs require large pre-labeled datasets as training sets, which are typically obtained through visual inspection. As mentioned earlier, this step can be time-consuming and negates some of the advantages of machine learning.

UML offers an alternative approach for galaxy morphological classification, eliminating the need for pre-labeled training sets. This characteristic renders it suitable for morphological analysis in the context of large-scale surveys (e.g., Schutter & Shamir 2015; Ralph 2019). Typically, UML methods involve two key steps: (1) feature extraction from raw images and (2) clustering galaxies with similar features. Numerous UML methods have already found application in various studies (e.g., Hocking et al. 2018; Fielding et al. 2022; Martin et al. 2020; Cheng et al. 2021). For instance, using a sample from the SDSS, Cheng et al. (2021) has demon-

strated the effectiveness of this UML approach for galaxy morphological classification, providing a robust scheme.

However, many UML methods only focus on one single clustering algorithm, potentially leading to inconsistent clustering outcomes when different similarity definitions are employed, which may result in misclassification. To obtain morphological classifications with high confidence, Zhou et al. (2022) introduced a Bagging-based multi-clustering model that incorporates three diverse clustering algorithms. This approach, combined with convolutional autoencoding (CAE; Massey et al. 2010) for feature extraction from images, yielded reliable classification results at the cost of excluding disputed sources with inconsistent voting. Subsequently, Fang et al. (2023) used the classification results from Zhou et al. (2022) as a training set in an SML algorithm to determine the morphological types of previously rejected sources from the same dataset. This framework that combines UML and SML methods for morphological classification (which is named as `USMORPH`) can help us obtain reliable and complete galaxy morphological type efficiently, which makes it suitable for future large-field sky surveys, such as the ones from CSST (Chinese Space Station Telescope, Zhan 2011, 2018), JWST (James Webb Space Telescope, Gardner et al. 2006), Euclid Space Telescope (Laureijs et al. 2011; Euclid Collaboration et al. 2022), Rubin Observatory (Blum et al. 2022), and Roman Space Telescope (Spergel et al. 2015).

In this work, we conduct a pilot study for CSST to validate the reliability of the algorithm developed by Zhou et al. (2022) and Fang et al. (2023) with COSMOS I-band images since these images are high-resolution and similar to the imaging data of the CSST. In brief, we perform our two-step algorithm to galaxies with $I_{\text{mag}} < 25$ at redshifts $0.2 < z < 1.2$ in the COSMOS field to get their morphological types. Additionally, both parametric and nonparametric morphologies for these galaxies are also estimated to investigate the consistency between our classification results and these morphological parameters. The results confirm that our classification results align with the expected relationships with the morphological parameters, underscoring the reliability of our algorithm.

The paper’s structure is as follows: In Section 2, an overview of the COSMOS program and our sample selection criteria are provided. Section 3 briefly introduces the methodology employed for galaxy morphological classification. Our classification results are presented in Section 4, followed by the conclusion in Section 5. Throughout this work, we adopt a flat Λ cold dark matter (Λ CDM) cosmology with $H_0 = 70 \text{ km s}^{-1} \text{ Mpc}^{-1}$, $\Omega_m = 0.3$, and $\Omega_\Lambda = 0.7$, along with a Chabrier (2003) initial mass function.

2. DATA SET AND SAMPLE SELECTION

2.1. COSMOS

The COSMOS field was strategically designed to explore the intricate connections between galaxy evolution, star formation, active galactic nuclei, dark matter, and large-scale structure within the redshift range $0.5 < z < 6$. This comprehensive survey spans a wide range of wavelengths,

from X-ray to radio, and covers an area of approximately 2 deg². In this study, the high-resolution images captured by HST/ACS in the F814W filter are capitalized, encompassing an area of roughly 1.64 deg² within the COSMOS field. This dataset represents the largest continuous field observed by HST ACS as yet. The original images comprise approximately 590 pointings, with an average exposure time of 2028 seconds per pointing. These images were meticulously processed by Koekemoer et al. (2007) using the STSDAS Multidrizzle package (Koekemoer et al. 2003), resulting in images with a pixel scale of 0''.03 and a 5 σ depth of 27.2 AB mag within a 0''.24 diameter aperture. In the subsequent analysis, all morphological measurements are based on these high-resolution HST I-band images.

2.2. COSMOS2020 Catalogue

The sample utilized in this study is constructed based on the ‘‘Farmer’’ COSMOS2020 catalog (Weaver et al. 2022), which provides comprehensive photometric information spanning 35 bands from ultraviolet to near-infrared. Weaver et al. (2022) further estimated some physical properties of galaxies in this field, including photometric redshift and stellar mass, through spectral energy distribution (SED) fitting with galaxy models, using this enhanced photometric dataset.

Redshifts were determined employing two distinct codes, EAZY (Brammer et al. 2008) and LePhare (Ilbert et al. 2006). For our analysis, we adopt the LePhare-derived redshifts, as Figure 15 of Weaver et al. (2022) illustrated their superior reliability within the magnitude range under consideration. Redshift estimation involves a library of 33 galaxy templates sourced from Bruzual & Charlot (2003) and Ilbert et al. (2009). Additionally, various dust extinction/attenuation curves are employed, encompassing the starburst attenuation curve introduced by Calzetti et al. (2000), the SMC extinction curve from Prevot et al. (1984), and two variations of the Calzetti law, including the 2175 Å bump. Then the photometric redshift (z_{LePh}) is defined as the median value derived from the redshift likelihood function.

Subsequently, with redshift fixed to z_{LePh} , the LePhare fitting code was executed once more to extract stellar mass and other pertinent physical properties. This stage considered Bruzual & Charlot (2003) stellar populations and a range of stellar formation histories (SFHs), including exponentially declining SFHs and delayed τ SFHs. For additional in-depth details, please refer to the works of Weaver et al. (2022) and Laigle et al. (2016).

2.3. Sample Selection

In this work, we have selected galaxies from the COSMOS2020 Catalog based on the following criteria: (1) $I_{mag} < 25$ mag, excluding galaxies that are too faint to obtain reliable morphological measurements; (2) $0.2 < z < 1.2$, ensuring that the morphology is estimated in the rest-frame optical band; (3) $FLAG_{COMBINE} = 0$, which means flux measurements are not influenced by bright stars and the objects are not on the edges of images, guaranteeing reliable

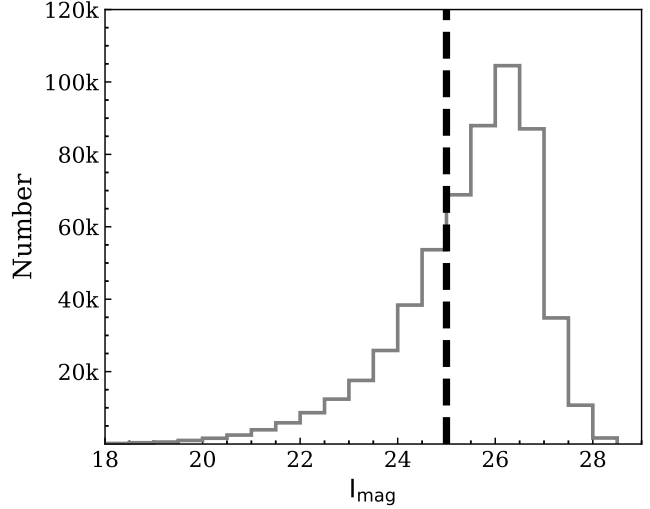


Figure 1. The distribution of I band magnitudes in the COSMOS field. A magnitude limit of $I_{mag} < 25$ is imposed.

photometric redshift and stellar mass estimations; (4) signal to noise ratio larger than 5 ($S/N > 5$), ensuring a real detection. Moreover, sources with bad pixels have also been excluded. As a result, the final sample comprises a total of 99,806 galaxies. The distribution of I-band magnitudes in the COSMOS field, along with the magnitude selection threshold of 25, is illustrated in Figure 1.

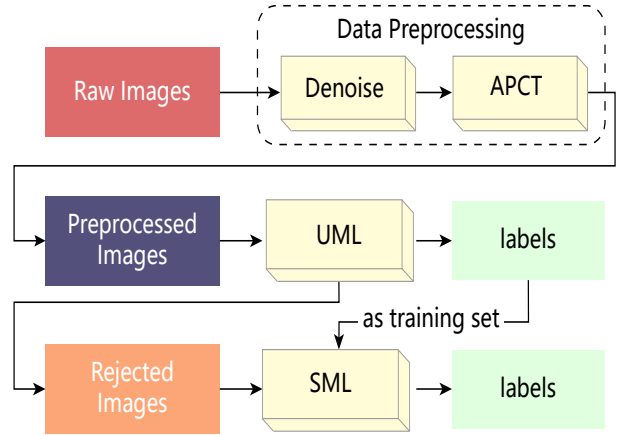


Figure 2. Framework of the morphological classification model employed in this work.

3. METHOD FOR MORPHOLOGICAL CLASSIFICATION

In this section, an overview of our U_{morph} algorithm employed for galaxy morphological classification is provided (as shown in Figure 2). This comprises three sections (data preprocessing, UML method, and SML method), and the detailed content is as follows.

3.1. Data Preprocessing

In our previous work, Zhou et al. (2022) employed a 28×28 -pixel cutout for each galaxy within the CANDELS field. However, given that the pixel scale of the COSMOS I-band images is $0''.03$ per pixel, which is notably finer than the $0''.06$ pixel scale in the CANDELS field, and that the redshift range considered in this study is quite lower than that of Zhou et al. (2022), larger 100×100 -pixel cutouts are generated for galaxies in our sample, with all galaxies centered in each cutout. To ensure that this cutout is sufficiently large to encapsulate adequate information for the majority of selected galaxies, we have checked that the half-light radius of approximately 97% of the galaxies in our sample is less than 0.12 arcsec (equivalent to 40 pixels). To prevent an excessively large cutout size, we have also checked and found that approximately 11% of galaxies have a half-light radius greater than 0.09 arcsec (30 pixels). To balance the training time and ensure most of the source information, we think this size is reasonable when considering that most cutouts (96%) contain only one galaxy. Moreover, before the following steps, a max-min normalization pretreatment is also applied to each cutout, following the methods described in Zhou et al. (2022).

We update the UML method developed in Zhou et al. (2022) by introducing some data preprocessing steps, enhancing the reliability of our results. Previously, some studies had shown that the distribution of image S/N can affect the performance of machine learning since noise can disturb image features and lead to misclassifications (Liu et al. 2022). Fortunately, Nazaré et al. (2018) had demonstrated that this problem can be overcome with noise reduction. CAE is demonstrated to be highly effective in noise reduction via automatically extracting image features and reconstructing images with the extracted features (e.g., Masci et al. 2011; Fang et al. 2023; Dai et al. 2023). In the CAE process, operations of convolution and pooling encode the pixels and give encoded features with a lower dimension. Then, denoised results can be obtained by applying deconvolution and unpooling to these features. To make our classification results more reliable, we also perform noise reduction with CAE to enhance the image quality of our samples. In our CAE algorithm, we consider 2 layers during the encoding process, each layer consisting of convolution and max-pooling operations. Then, through a fully connected layer, we represent the features of galaxies as a 40-dimensional vector. The decoding process is the inverse of the encoding process, and the configurations used during encoding and decoding are identical. An schematic diagram of this process can be found in Figure 2 of Zhou et al. (2022). We build our algorithm based on TensorFlow¹(Abadi et al. 2016). During the convolution operations, the channel size is set to 16 with a kernel size of 5×5 . Subsequently, in the max-pooling process, a 2×2 pixel block is consolidated into a

single pixel. Due to memory constraints, the batch size is set to 8. The activation function is the Rectified Linear Unit function (Agarap 2018), while the loss function is the Mean Square Error (Lehmann & Casella 2006). We also employ a learning rate scheduler (Exponential Decay, Li & Arora 2019) to dynamically adjust our learning rate, starting with an initial value of 3×10^{-4} . We do not use batch normalisation, or dropout, or regularisation in this work. We train our program for 32 epochs, extending the training by approximately 10 additional epochs beyond the point where the validation loss plateaued to get a better denoising effect. Figure 3 provides a visual comparison before and after noise reduction: in the left column, raw images of randomly selected galaxies from our sample are presented, and in the middle column, the results after noise reduction are showcased. It is evident that the image quality is substantially improved after noise reduction while retaining the essential morphological features.

Furthermore, a number of groups point out that the standard CNN models have poor robustness to rotations of images, which may lead to misclassification of the galaxy morphological type after rotation (e.g., Chiu et al. 2018; Yao et al. 2019). To overcome this shortcoming, Fang et al. (2023) proposed an adaptive polar coordinate transformation (APCT) method in the data preprocessing procedure. Compared to traditional data augmentation and conventional polar coordinate unwrapping, Fang et al. (2023) found that APCT can significantly improve the accuracy of CNNs when images are rotated. Moreover, by ignoring information about image orientation, APCT can make models focus on other more important features of galaxies, which makes it an important preprocessing method. Here we provide a brief introduction to this method (see Fang et al. 2023 for more details). Essentially, the pixels with the maximum and minimum flux values in the images are identified as the brightest and darkest points, respectively. Subsequently, the line connecting the brightest and darkest points is designated as the polar axis. Then, the axis is rotated counterclockwise by an increment of 0.05 rad each time. For each discrete rotation, the axis traverses numerous pixels of the raw images. By stacking the pixels along this rotating axis while rotating, the entire image can be unfolded into polar coordinates. Finally, the images are mirrored to highlight morphological features since CNN is more sensitive to information at the center of the image. To make our results rotationally invariant, We apply this method to our samples. In the right column of Figure 3, we present the corresponding results after implementing APCT.

3.2. UML Process

After completing the data preprocessing steps, we apply the UML method, as outlined in Zhou et al. (2022), to obtain classification results for some of our samples. The UML method comprises two main steps: (1) Using the images processed with noise reduction and APCT, relevant features

¹ <https://www.tensorflow.org>

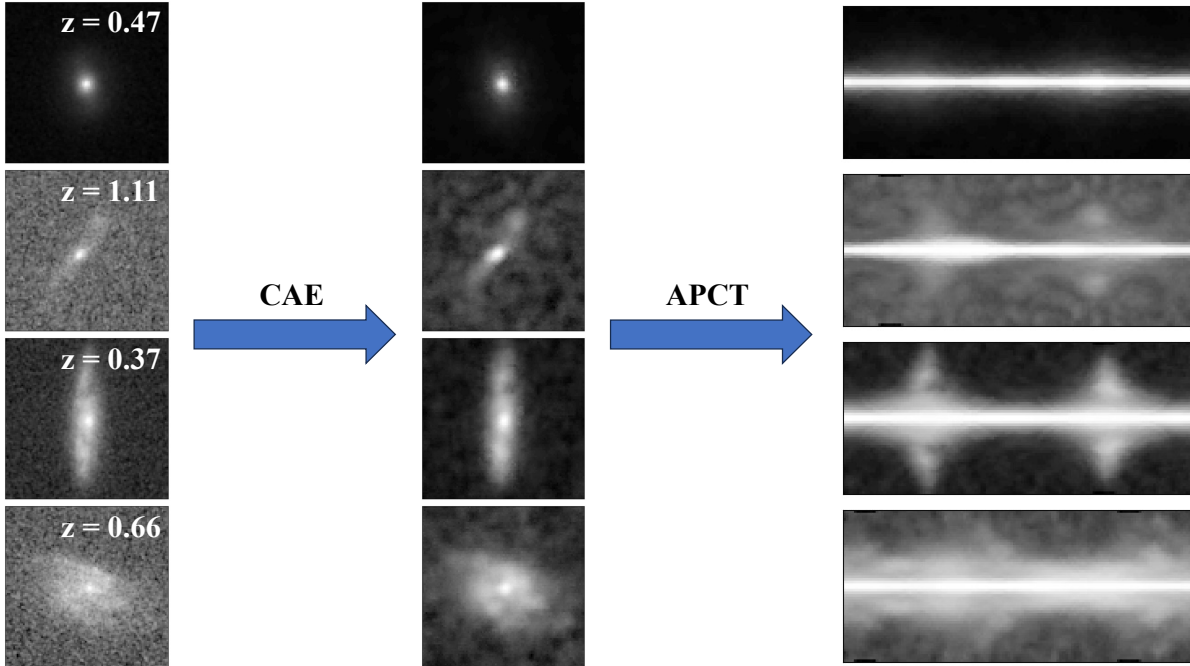


Figure 3. Some examples of image preprocessing, the left column displays original images of four randomly selected galaxies, the middle column shows the corresponding denoised images, and the right column displays images that have undergone a polar coordinate transformation. The redshift information of these chosen galaxies is shown in the first column.

are extracted with CAE², then these extracted 40-dim features are used for the next step; (2) a bagging-based multi-clustering approach is employed to cluster galaxies with similar features into distinct groups. In this second step, three different clustering models are employed simultaneously: the k-means clustering algorithm (Hartigan & Wong 1979), the agglomerative clustering algorithm (Murtagh 1983; Murtagh & Legendre 2014), and the Balanced Iterative Reducing and Clustering using Hierarchies (BIRCH) algorithm (Zhang et al. 1996). The sample is clustered into 50 categories by each model separately. By setting the K-means labels as the primary labels, we assign labels to the groups of other models according to the highest frequency of the K-means label in that group. Then, the “majority wins” strategy is used in voting. The sources that the three models reach a consensus in voting are retained, while those that do not reach a consensus are discarded. This voting strategy can improve the clustering quality, thereby leading to a more reliable classification, as demonstrated in Zhou et al. (2022) and liu et al. (2023).

After removing galaxies with inconsistent voting results, 36,604 galaxies are neatly grouped into 50 groups. The morphological type of these 50 groups is determined through post-hoc visual inspection for label alignment (refer to liu et al. 2023 for further details). Specifically, owing to the

high purity of the clustering, galaxies within each group exhibit similar features. Consequently, the morphological type for a particular group can be obtained by visually inspecting only a subset of galaxies from that group. In this study, we randomly select 100 galaxies from each group for visual inspection. By evaluating the overall morphological features of these randomly selected 100 samples simultaneously, we categorize each group into one of five types: SPH, ETD, LTD, IRR, and UNC. Finally, these 36,604 galaxies are classified into five distinct categories: SPHs (8233), ETDs (5322), LTDs (6320), IRRs (9468), and UNCs (7261). Figure 4 illustrates an example of this process.

3.3. SML Process

By excluding 63,202 sources with inconsistent voting results, a set of 36,604 galaxies with reliable morphological labels are obtained through our UML clustering process. Then these 36,604 well-classified sources are used as a training set to conduct SML for the remaining 63,202 galaxies. Based on the findings of Fang et al. (2023), who demonstrated that GoogLeNet performs well in classifying deep-field galaxies, we employ the GoogLeNet algorithm (Szegedy et al. 2015) as a supervised classification model.

To prevent overfitting, the labeled galaxies are randomly divided into a 9:1 ratio of training set (32,944) and validation set (3660), following the same proportion as in Fang et al. (2023). To ensure the robustness of our GoogleNet model, we also examined the distribution of morphological types in the training and validation sets. The results are shown in Figure 5, from which it can be clearly seen that these two sets

² In the preprocessing part, we use CAE to perform noise reduction. In this step, we run CAE once more to extract features. The configuration of CAE used here for feature extraction is the same as the one used for noise reduction

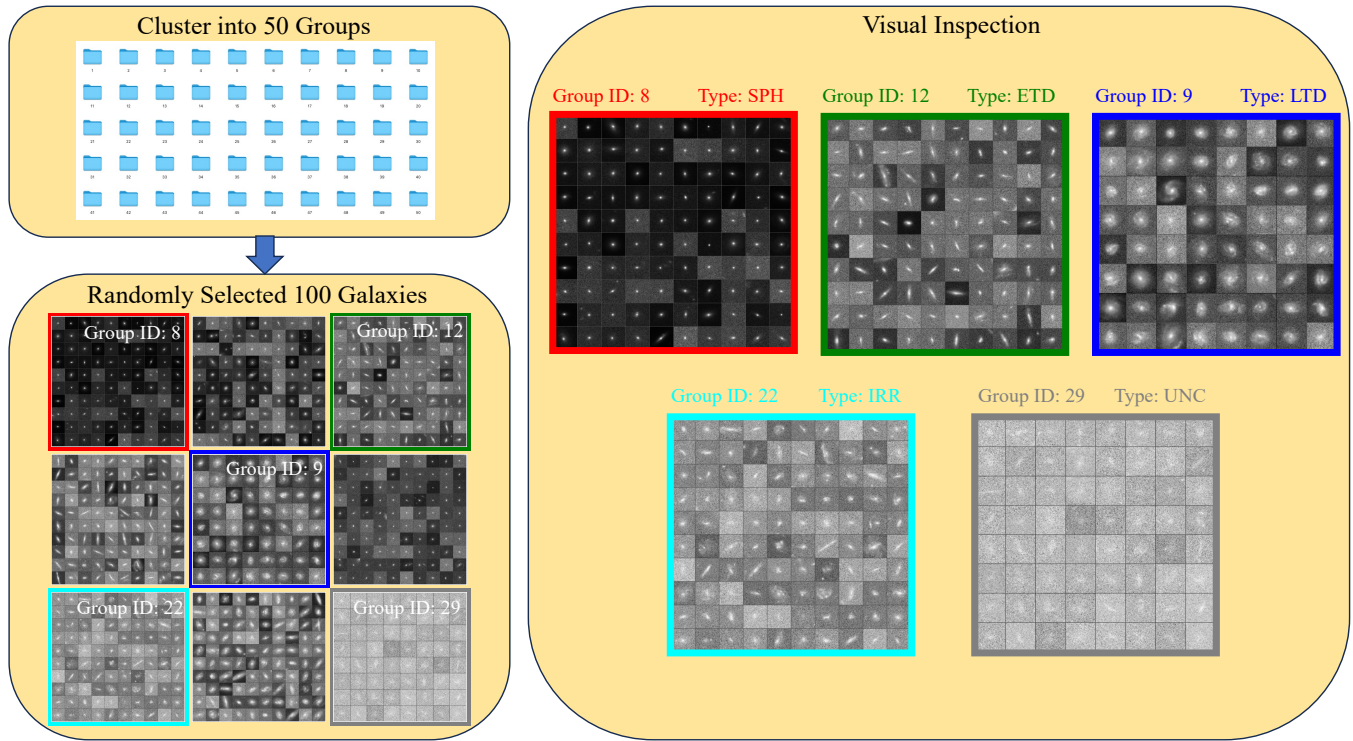


Figure 4. Illustration of the post-hoc visual inspection for label alignment. 100 galaxies are randomly selected from each group (only 64 galaxies are selected for Group 9 because the total number of galaxies in this group is less than 100) for visual inspection. Since galaxies within each group share similar features, we are able to quickly categorize each group into five types (SPH, ETD, LTD, IRR, and UNC) by simultaneously assessing the overall morphological features of these selected galaxies.

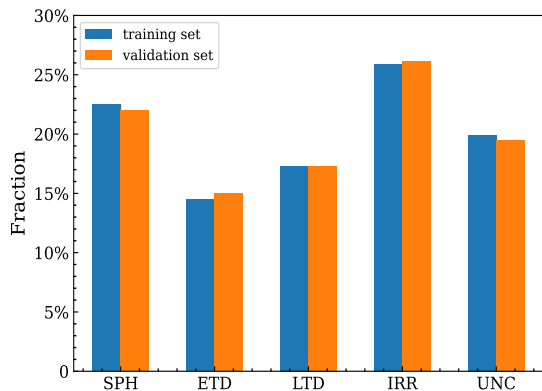


Figure 5. The distribution of galaxy morphological types in the training and validation sets.

have the same distribution of morphological types. Additionally, we have also examined the distribution of the training set and validation set in some other physical parameter (including M_* , redshift, and some other morphological parameters) space and find that they also exhibit similar distributions. Figure 6 displays the precision and recall rates of the GoogLeNet model, which is estimated based on the validation set. It is evident that the overall accuracy rate is approximately 94%, indicating that GoogLeNet performs well in classifying galaxies of all types. With this SML method,

Table 1. The number of galaxies classified into different types

TYPE	SPH	ETD	LTD	IRR	UNC	TOTAL
UML	8233	5322	6320	9468	7261	36,604
SML	6967	12,047	14,823	19,497	9868	63,202
TOTAL	15,200	17,369	21,143	28,965	17,129	99,806

we obtain morphological classifications for the remaining 63,202 galaxies.

4. RESULTS AND DISCUSSION

4.1. Overall morphological classification results

In preparation for future large-scale surveys, there is a growing demand for efficiently obtaining morphological information for a significant number of galaxies within a short time frame. In this study, we have successfully classified the morphologies of approximately 100,000 galaxies in the COSMOS field using I-band images, which include 15,200 SPHs, 17,369 ETDs, 21,143 LTDs, 28,965 IRRs, and 17,129 UNC. Detailed classification results are shown in Table 1. The whole task (both UML and SML) is completed within

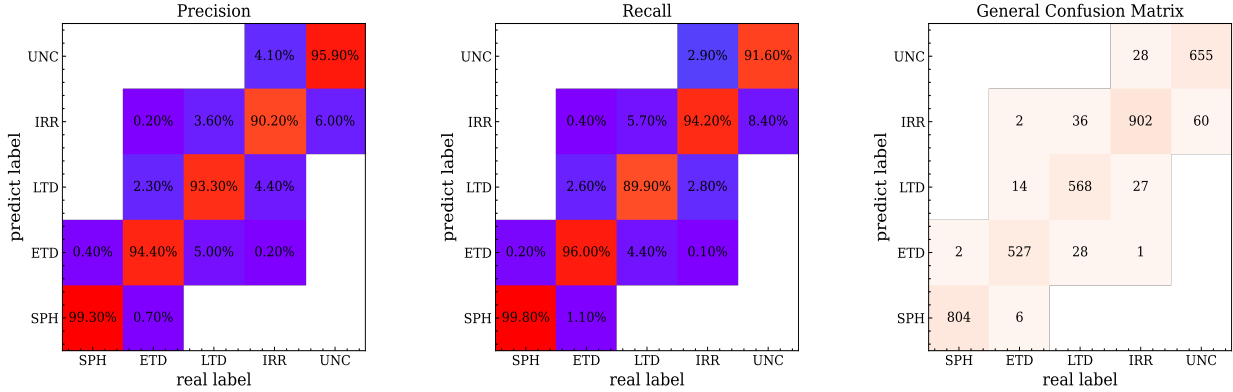


Figure 6. The left and middle panels represent the precision and recall of the GoogleNet model, with both overall precision and recall exceeding 94%, indicate that the GoogleNet model can effectively distinguish between different types of galaxies. The right panel represents the general confusion matrix.

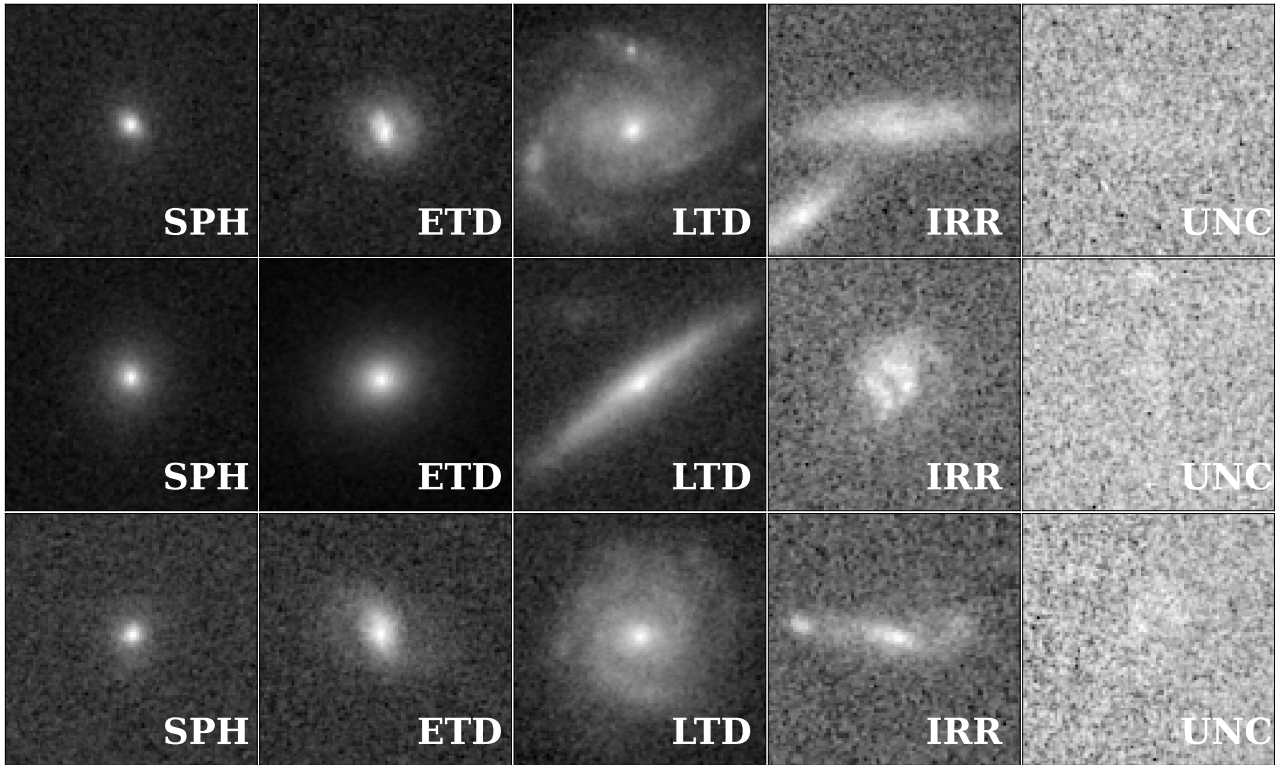


Figure 7. Some examples of the final classification results. From left to right, they are SPHs, ETDs, LTDs, IRRs, and UNC.

less than one day, which means this method has potential for application in future large-field sky surveys.

To test our classification, we conduct visual inspections on a randomly sampled subset of samples from the final results. The visual examination confirms that SPHs tend to be compact and bulge-dominated, whereas LTDs exhibit extended structures with disk dominance. Some LTDs also display prominent spiral arm structures. ETDs are characterized by their relatively less compact form with a bright nuclear region and a disk component. IRRs encompass galaxies with irregular structures or merger signatures. UNC.

galaxies that cannot be confidently identified due to poor S/Ns. Some examples of the classification results are presented in Figure 7, which demonstrates the effectiveness of our algorithm in distinguishing galaxies with different morphological types.

Furthermore, the t-distributed Stochastic Neighbor Embedding (t-SNE) technique is adopted to assess the classification results, which maps high-dimensional data into a two- or three-dimensional space, making it suitable for visualization and inspection (van der Maaten & Hinton 2008). To enhance clarity, 5000 randomly selected galaxies are presented

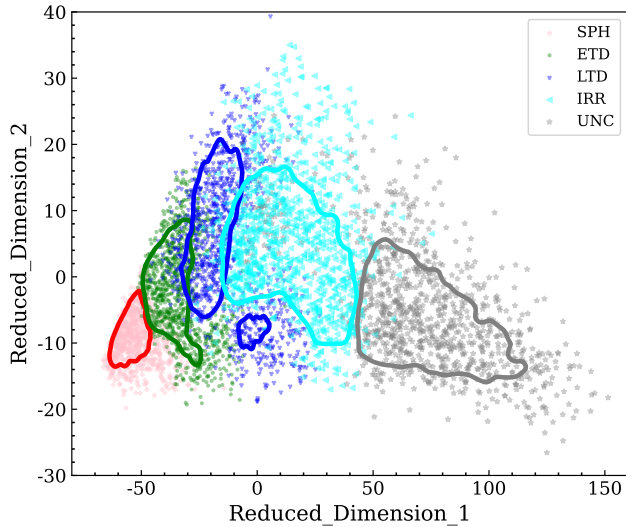


Figure 8. The t-SNE diagram of randomly selected 5000 galaxies from the final classification result, where red, green, blue, cyan, and grey represent SPHs, ETDs, LTDs, IRRs, and UNC, respectively. Additionally, unless otherwise stated, the same color scheme is adopted in the following analyses. The solid lines of different colors in the figure represent the corresponding 1 sigma contours. Different types of galaxies exhibit distinct boundaries on the t-SNE diagram, indicating that our classification algorithm can effectively distinguish between different types of galaxies.

using the t-SNE technique in Figure 8, which is based on the extracted 40-dim features in the UML process. Considering that the axes do not have corresponding physical meanings, here we simply use “Reduced_Dimension_1” and “Reduced_Dimension_2” to represent the axis labels. The solid lines of different colors in the figure represent the corresponding 1 sigma contours. This figure reveals distinct boundaries between different galaxy types, indicating that each class of galaxies in our classification indeed possesses distinct characteristics. We note that LTDs appear to be divided into two parts in the t-SNE diagram, which may be attributed to projection effects. There is also overlaps between different groups. This may also be caused by the morphological similarities between different groups, which is expected by galaxy evolution scenario. Since the t-SNE diagram can only provide a qualitative overview of the results, we will further validate our classification results in the following sections.

4.2. Test of Morphological Parameters

The structural parameters of galaxies are closely related to their morphological types. For example, it is commonly accepted that elliptical galaxies tend to have Sérsic index greater than 2, while disk galaxies typically exhibit Sérsic index less than 2 (e.g., Fisher & Drory 2008; Blanton & Moustakas 2009). Nonparametric structural parameters also offer valuable insights into galaxy morphological types, as differ-

ent galaxy categories often occupy distinct positions in parameter space (e.g., Lotz et al. 2008; Yao et al. 2023).

In this section, we investigate the classification results using galaxy morphological parameters. Since extensive researches have already explored the correlations between morphologies and other morphological parameters (e.g., Gu et al. 2018; Zhou et al. 2022; Dai et al. 2023), our analysis focuses exclusively on massive galaxies with stellar masses exceeding $10^9 M_\odot$. We exclude the UNC subclass from our analysis due to the difficulty in measuring morphological parameters for these galaxies, primarily stemming from their relatively low S/Ns.

4.2.1. Parametric Measurements

In this study, the measurements of parametric morphology for galaxies in the COSMOS field are conducted using the GALAPAGOS software (Barden et al. 2012; Häußler et al. 2022), which serves as a wrapper for both SExtractor (Bertin & Arnouts 1996) and GALFIT (Peng et al. 2002). The software utilizes a single Sérsic model to fit the surface brightness profile of each galaxy and measure their Sérsic index and effective radius (r_e).

To ensure the reliability of our analysis and eliminate the influence of galaxies that cannot be fully covered by our 100×100 pixel cutout, we excluded galaxies for which the estimated r_e exceeded 40 pixels. This removal affects less than 5% of our galaxy sample, demonstrating that it had no significant impact on our results.

The left panel of Figure 9 illustrates the distribution of effective radius for four galaxy subclasses: SPHs, ETDs, LTDs, and IRRs. The median effective radius for these subclasses are 1.77, 2.33, 3.18, and 3.90 kpc, respectively. Notably, SPHs tend to have smaller sizes compared to the other subclasses, and the effective radius increases in the order from SPHs to ETDs, LTDs, and IRRs. The right panel of Figure 9 presents the distributions of Sérsic indices for the same four galaxy subclasses. SPHs exhibit a higher degree of compactness with a median Sérsic index of 4.34, whereas ETDs, LTDs, and IRRs have median Sérsic index of 1.94, 1.18, and 0.88, respectively. In summary, the distributions of Sérsic index and effective radius for different galaxy types align with our expectations regarding the relationships between galaxy types and structural parameters.

4.2.2. Nonparametric Measurements

Since the morphological structures of high-redshift galaxies are likely to be irregular, it can be challenging to fit the brightness distribution of these high-redshift galaxies with empirical functions. Therefore, some nonparametric morphological parameters are developed to describe various features of galaxies. The most widely used parameters are CAS statistics. C (concentration) is developed to quantify the concentration of light within a galaxy’s central region compared to its outer regions (e.g., Bershady et al. 2000; Conzelice 2003). A (asymmetry) could characterize the degree of asymmetry exhibited by a galaxy after a 180° rotation (e.g.,

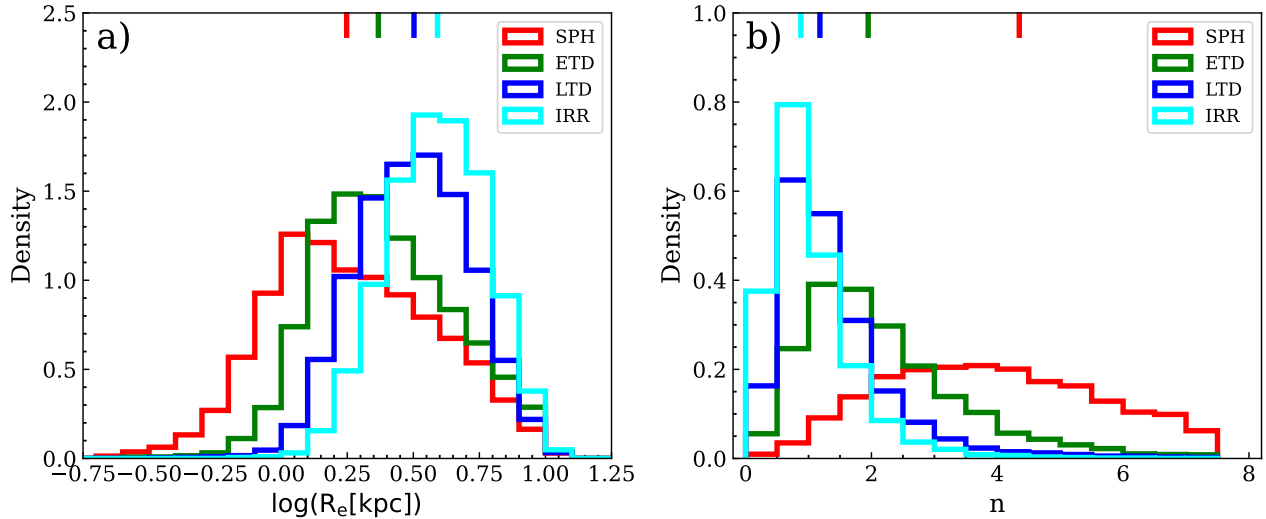


Figure 9. The distribution of effective radius (left panel) and Sérsic index (right panel) for different types of galaxies. The bars at the top represent the median values of $\log(r_e)$ and n for different galaxy types. It is evident that from SPHs to IRRs, the effective radius of galaxies gradually increases, while the Sérsic index gradually decreases.

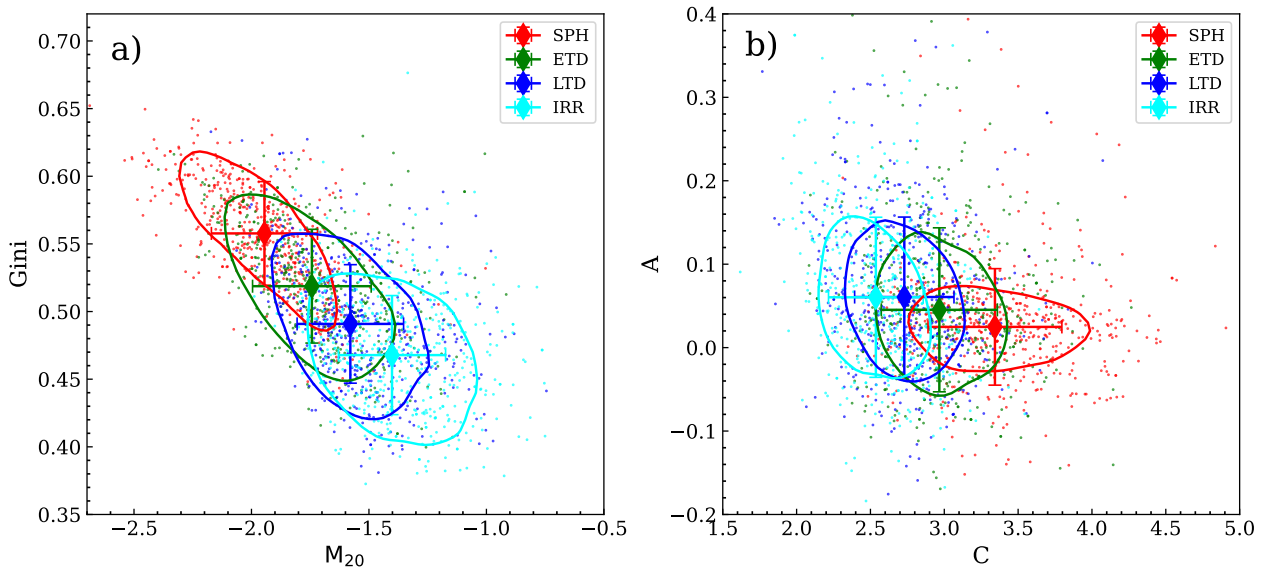


Figure 10. The distribution of four subclasses in the Gini- M_{20} (left) and C-A (right) space. The contour represents 50% of the specified galaxies. The diamonds with different colors correspond to the median values of the parameters and the error bars represent the corresponding standard deviations.

Conselice et al. 2000; Conselice 2003). S (clumpiness) represents the proportion of light in a galaxy that is distributed in clump patterns. Besides the CAS system, the Gini- M_{20} system has also been adopted in many works. Gini coefficient represents the distribution of light within a galaxy and a higher value indicates a more unequal distribution (e.g., Lotz et al. 2004, 2008). M_{20} (the normalized second-order moment of the brightest 20% of the galaxy’s flux) indicates whether light is concentrated in a galaxy, and a more concentrated result (a more negative M_{20}) does not imply that light is central concentration, instead, the light may be concen-

trated in any location within the image (e.g., Lotz et al. 2004, 2008). More recently, a new suit of parameters was introduced by Freeman et al. (2013), that includes M (multimode, which quantifies the area ratio between two most “prominent” clumps within a galaxy), I (intensity, which represents the light ratio between the two brightest subregions within a galaxy.), and D (Deviation, which represents the distance between the image light-weighted center and the brightest peak.)

Rodriguez-Gomez et al. (2019) had developed a python package `statmorph` for calculating the nonparametric

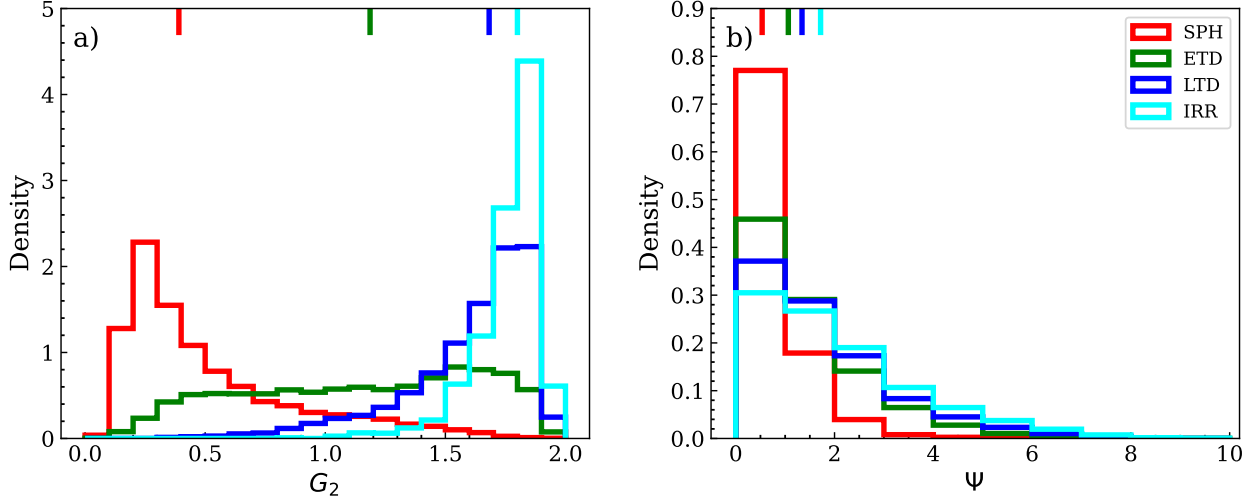


Figure 11. The distribution of G_2 (left panel) and Ψ (right panel) for different types of massive galaxies. The bars at the top represent the median values of the corresponding parameters.

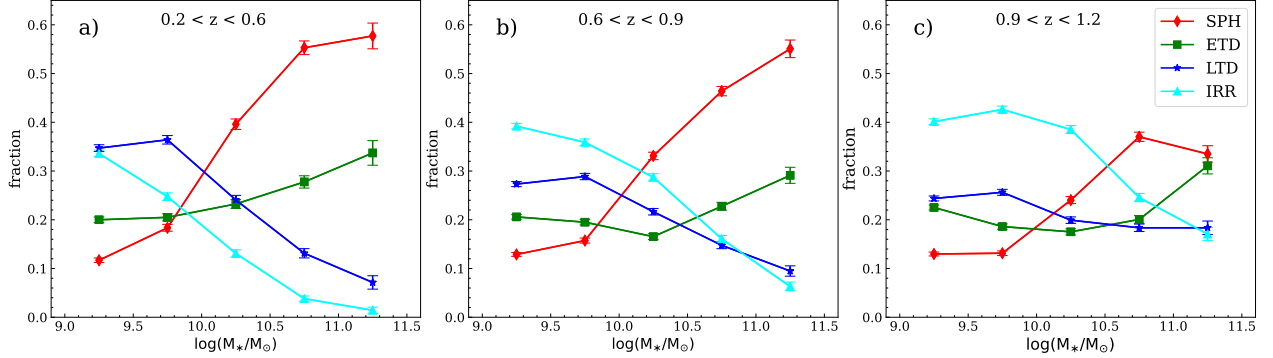


Figure 12. The proportion of different types of galaxies as a function of stellar mass, with different panels displaying the results at different redshifts bins (panel a: $0.2 < z < 0.6$; panel b: $0.6 < z < 0.9$; panel c: $0.9 < z < 1.2$).

morphology of galaxies, including Gini, M_{20} , C, A, S, M, I, and D. Based on this package, Yao et al. (2023) had optimized the code with Cython (Behnel et al. 2011) and increased the calculation speed by one order of magnitude, which is suitable for the large-scale survey. In addition, Yao et al. (2023) had also incorporated some additional optional parameters into statmorph, including the color dispersion (ξ ; Papovich et al. 2003), Multiplicity (Ψ ; Law et al. 2007), and the second gradient moment (G_2 ; Rosa et al. 2018). The improved code has been named statmorph_csst. The reliability of statmorph has been extensively validated in previous studies. Yao et al. (2023) conducted tests to compare measurement results between statmorph_csst and the original statmorph. The results, presented in their Appendix 1, indicate that the optimization has virtually no impact on the measured results of morphological parameters, underscoring the reliability of statmorph_csst. In this study, the nonparametric structural parameters of galaxies in the COSMOS field are esti-

mated using the statmorph_csst code, which requires only a few hours of computational time.

Considering that the measurement of nonparametric structural parameters is influenced by S/Ns, previous studies (e.g., Lotz et al. 2004, 2006, Treu et al. 2023, Yao et al. 2023) have shown that reliable measurements of these parameters can be obtained when the average S/N per pixel ($\langle S/N \rangle$) exceeds 2. Thus, we focused our analysis on galaxies with $\langle S/N \rangle$ greater than 2 in this part. The detailed method of obtaining $\langle S/N \rangle$ is described in Section 4.3.2 of Rodriguez-Gomez et al. (2019).

In Figure 10, we present the distribution of four galaxy subclasses in the Gini- M_{20} (left) and C-A (right) parameter spaces. Since these parameters are widely used in many studies, we do not introduce the definitions of these parameters, which have been carefully described in Section 4 of Rodriguez-Gomez et al. (2019). The contours in this figure represent 50% of the specified galaxies. Different colored diamonds correspond to the median parameter values for different types of galaxies, with error bars indicating the corresponding standard deviations. It is evident from the left panel

that galaxies transition from SPHs to IRRs with a gradual decrease in Gini and a simultaneous increase in M_{20} , which aligns with our common understandings of Gini and M_{20} for different galaxy types. When focusing on the C-A space, numerous studies have shown that more compact galaxies tend to have larger C coefficients, while more symmetric galaxies tend to have smaller A coefficients. From the right panel, it is evident that the more compact and symmetric SPHs exhibit larger C values and smaller A values, while the more diffuse and irregular IRRs exhibit smaller C values and larger A values, although the difference between A values is small. This is consistent with some previous studies (e.g., Lotz et al. 2004, 2006; Conselice et al. 2008; Conselice 2014). These findings support the consistency of our classification results with nonparametric parameters.

In addition to these commonly used parameters, some less commonly used but also useful parameters are estimated. In Figure 11, we present the distribution of G_2 (left panel) and Ψ (right panel) parameters for different types of galaxies.

The G_2 is designed by Rosa et al. (2018) to distinguish between elliptical and spiral galaxies based on the symmetry of the flux gradient. By denoting the flux at coordinates (x_i, x_j) in an image as $I(x_i, x_j)$, the local gradient vectors $V(i, j)$ at (x_i, x_j) can be estimated by calculating the first-order partial of $I(x_i, x_j)$, assuming that the distance between adjacent pixels in the same direction is 1. Based on a given tolerance for norm and phase, symmetric pairs are defined as those that are concentric and have the same modulus and a phase shifted by π . Then, asymmetric vectors v_k can be obtained after removing all the symmetric pairs from the local gradient vectors. Thus, the G_2 coefficient is defined as:

$$G_2 = \frac{V_A}{V} \times \left(2 - \frac{|\sum_{k=1}^{V_A} v_k|}{\sum_{k=1}^{V_A} |v_k|} \right) \quad (1)$$

where V is the number of local gradient vectors and V_A is the number of asymmetric vectors. $|\sum_{k=1}^{V_A} v_k|$ is the modulus of the sum of asymmetric vectors, while $\sum_{k=1}^{V_A} |v_k|$ is the sum of the modulus of asymmetric vectors.

The left panel of Figure 11 displays the distribution of G_2 for different galaxy subclasses. Similar to Figure 9, the bars at the top indicate the median values of G_2 for each subclass. Galaxies exhibit increasing asymmetry in their flux gradient from SPHs to IRRs, with median G_2 values of 0.39, 1.19, 1.68, and 1.80 for SPHs, ETDs, LTDs, and IRRs, respectively. With a sample from SDSS, Rosa et al. (2018) found that elliptical and spiral galaxies exhibit a clear bimodal distribution in G_2 , where the G_2 value of spiral (elliptical) galaxies is typically larger (smaller) than 1. Assuming that SPHs are elliptical galaxies and LTDs are spiral galaxies, a similar trend has also been seen in this work. However, ETDs exhibit G_2 values that span a wide range, possibly due to their combined bulge and disk structures. Therefore, for galaxies at middle redshift ($z \sim 1$), G_2 coefficient is also available to distinguish between bulge- and disk-dominated galaxies, but for galaxies with interim morphologies, it should be treated more carefully.

Furthermore, Ψ was introduced by Law et al. (2007) to describe how the light distribution of galaxies can be decomposed into apparent components, similar to M_{20} . In general, galaxies that appear more clumpy tend to have larger Ψ values. By using flux as a proxy for “mass”, the “potential energy” of the observed flux distribution is defined as:

$$\psi_{actual} = \sum_i \sum_j \frac{X_i X_j}{r_{ij}} \quad (2)$$

where X_i and X_j are fluxes of the i th and j th pixels, and r_{ij} is the distance (in pixels) between the i th and j th pixels. Then the pixels of raw images are rearranged in a circular configuration that the brightest pixel is at the center, and the flux of the other pixels gradually decreases with distance, which is considered the most compact configuration. The distance between the i th and j th pixels on this rearranged map is represented as r'_{ij} . Then the “potential energy” of this rearranged flux distribution is:

$$\psi_{compact} = \sum_i \sum_j \frac{X_i X_j}{r'_{ij}}. \quad (3)$$

The Ψ coefficient is then defined as:

$$\Psi = 100 \log_{10} \frac{\psi_{compact}}{\psi_{actual}}. \quad (4)$$

The distribution of the Ψ parameter is displayed in the right panel of Figure 11. There is an increasing trend of Ψ from SPHs to IRRs. The median Ψ values are 0.53, 1.06, 1.34, and 1.72 for SPHs, ETDs, LTDs, and IRRs, respectively. Considering that IRRs are much more clumpy than SPHs, this figure demonstrates that our classification is consistent with Ψ .

4.3. Test of Physical Properties

Many studies have already shown that there is a close connection between galaxy morphologies and their physical properties. It is now widely agreed that as the stellar mass increases, galaxies become more bulge-dominated (e.g., Cheng et al. 2020; Du et al. 2021), and galaxies at higher redshift are more likely irregular (e.g., Tohill 2021; Kartaltepe et al. 2023). In this section, we also select galaxies with stellar masses larger than $10^9 M_\odot$ to study the relationship between galaxy morphologies and their physical properties.

In Figure 12, the number fractions of galaxies for each morphology class are presented as a function of stellar mass at three different redshift bins (panel a: $0.2 < z < 0.6$; panel b: $0.6 < z < 0.9$; and panel c: $0.9 < z < 1.2$). The symbols, including diamonds, squares, stars, and triangles, represent the fractions of SPHs, ETDs, LTDs, and IRRs, respectively, within different stellar mass bins.

In each panel, it is evident that as the stellar mass of galaxies increases, the proportions of SPHs and ETDs gradually rise, while the proportions of LTDs and IRRs decrease. Similar results were also shown in the work of Huertas-Company

et al. (2013), where at the high-mass end, galaxies are dominated by early-type morphology, while at the low-mass end, galaxies are dominated by late-type morphology. Combining with our earlier discussion (Section 4.1) where both SPHs and ETDs exhibit a nuclear bulge structure, while LTDs and IRRs do not have such a structure, this trend suggests that an increase in galaxy stellar mass is accompanied by an increase in bulge dominance.

Comparing the results across different panels, it's also clear that with increasing redshift, the proportion of IRRs continues to increase, while the proportion of SPHs decreases, especially for galaxies with larger M_* . Buitrago et al. (2013) found a similar trend, with the proportions of SPHs was approximately 40% for massive galaxies at $z \sim 1$, but this proportion increased to 60% at $z \sim 0.2$. This might indicate that over cosmic time, galaxies tend to evolve toward more regular morphologies. However, at the lower mass end, the change in the ratio of IRRs to SPHs is less pronounced, with SPHs comprising approximately 10% and IRRs approximately 30%. This difference could be attributed to lower-mass galaxies being more susceptible to perturbations, such as tidal interactions, ram pressure, and stellar feedback, which can lead to a more irregular appearance. In summary, these results underscore the complex interplay between galaxy morphology, stellar mass, and redshift.

5. SUMMARY

In this work, utilizing the galaxy morphology classification algorithm (`USmorph`) that combines UML and SML methods, as proposed by Zhou et al. (2022) and Fang et al. (2023), we classify nearly 100,000 galaxies in the COSMOS field into five categories: SPHs (15,200), ETDs (17,369), LTDs (21,143), IRRs (28,965), and UNCs (17,129) using HST/ACS I-band images. In visual inspection, SPHs exhibit a clear bulge-dominated structure, while LTDs display a clear disk structure. ETDs show a disk structure but have bulge components as well. IRRs include galaxies with irregular structures or merger evidence, while galaxies that could not be confidently identified due to poor S/Ns are classified as UNCs.

Furthermore, we estimate the morphological parameters of these galaxies and find that the relationship between our classification results and galaxy morphological parameters for

massive galaxies is consistent with our expectations. In brief, as galaxies transition from IRRs to SPHs, their Sérsic index gradually increases, and their effective radius decreases. When considering nonparametric morphologies, more compact galaxies (e.g., SPHs) exhibit larger Gini and C coefficients, while more diffuse galaxies (e.g., IRRs) exhibit larger M_{20} , A, and Ψ coefficients. In addition, G_2 has also been proven to effectively distinguish SPHs from LTDs. Moreover, the relationship between galaxy morphology and their physical properties is investigated using our classification results. A clear relationship was observed between the morphology of galaxies and their stellar mass and redshift. Relevant information is catalogued in the electronic version of the article, and we show a part of the catalog in Table 2.

The forthcoming CSST will be launched in 2024. With a 2-meter aperture and a large field of view, CSST is planned to conduct a 15,000 deg² multi-band deep field survey with an expected 5σ depth of $r = 26.0$ mag and a 400 deg² ultra-deep field survey with an expected 5σ limiting magnitude of $r = 27.2$ mag (Zhan 2011, 2018). This will provide us with a large number of high-resolution images. Meanwhile, the `USmorph` algorithm can classify about 30,000 galaxies per hour, which could meet the requirements of the CSST surveys. This will help us better utilize future CSST image data for studying galaxy morphology.

This work is supported by the Strategic Priority Research Program of Chinese Academy of Sciences (Grant No. XDB 41000000), the National Science Foundation of China (NSFC, Grant No. 12233008, 11973038), the China Manned Space Project (No. CMS-CSST-2021-A07) and the Cyrus Chun Ying Tang Foundations. Z.S.L. acknowledges the support from Hong Kong Innovation and Technology Fund through the Research Talent Hub program (GSP028). Y.Z.G. acknowledges support from the China Postdoctoral Science Foundation funded project (2020M681281). C.C.Z. acknowledges the support from National Natural Science Foundation of China (NSFC, Grant No. 62106033). S.B. acknowledges the support from Scientific Research Fund Project of Yunnan Provincial Department of Education (2023Y1040).

REFERENCES

- Abadi, M., Agarwal, A., Barham, P., et al. 2016, arXiv e-prints, arXiv:1603.04467, doi: [10.48550/arXiv.1603.04467](https://doi.org/10.48550/arXiv.1603.04467)
- Agarap, A. F. 2018, arXiv e-prints, arXiv:1803.08375, doi: [10.48550/arXiv.1803.08375](https://doi.org/10.48550/arXiv.1803.08375)
- Banerji, M., Lahav, O., Lintott, C. J., et al. 2010, MNRAS, 406, 342, doi: [10.1111/j.1365-2966.2010.16713.x](https://doi.org/10.1111/j.1365-2966.2010.16713.x)
- Barden, M., Haußler, B., Peng, C. Y., McIntosh, D. H., & Guo, Y. 2012, Monthly Notices of the Royal Astronomical Society
- Behnel, S., Bradshaw, R., Citro, C., et al. 2011, Computing in Science & Engineering, 13, 31, doi: [10.1109/MCSE.2010.118](https://doi.org/10.1109/MCSE.2010.118)
- Bershady, M. A., Jangren, A., & Conselice, C. J. 2000, The Astronomical Journal, 119, 2645, doi: [10.1086/301386](https://doi.org/10.1086/301386)
- Bertin, E., & Arnouts, S. 1996, Astronomy and Astrophysics Supplement Series, 117, 393, doi: [10.1051/aas:1996164](https://doi.org/10.1051/aas:1996164)
- Blanton, M. R., & Moustakas, J. 2009, Annual Review of Astronomy and Astrophysics, 47, 159, doi: [10.1146/annurev-astro-082708-101734](https://doi.org/10.1146/annurev-astro-082708-101734)

- Blum, B., Digel, S. W., Drlica-Wagner, A., et al. 2022, arXiv e-prints, arXiv:2203.07220, doi: [10.48550/arXiv.2203.07220](https://doi.org/10.48550/arXiv.2203.07220)
- Brammer, G. B., Van Dokkum, P. G., & Coppi, P. 2008, *The Astrophysical Journal*, 686, 1503, doi: [10.1086/591786](https://doi.org/10.1086/591786)
- Bruzual, G., & Charlot, S. 2003, *Monthly Notices of the Royal Astronomical Society*, 344, 1000, doi: [10.1046/j.1365-8711.2003.06897.x](https://doi.org/10.1046/j.1365-8711.2003.06897.x)
- Buitrago, F., Trujillo, I., Conselice, C. J., & Häußler, B. 2013, *MNRAS*, 428, 1460, doi: [10.1093/mnras/sts124](https://doi.org/10.1093/mnras/sts124)
- Calzetti, D., Armus, L., Bohlin, R. C., et al. 2000, *The Astrophysical Journal*, 533, 682, doi: [10.1086/308692](https://doi.org/10.1086/308692)
- Cassata, P., Guzzo, L., Franceschini, A., et al. 2007, *ApJS*, 172, 270, doi: [10.1086/516591](https://doi.org/10.1086/516591)
- Cavanagh, M. K., Bekki, K., & Groves, B. A. 2021, *MNRAS*, 506, 659, doi: [10.1093/mnras/stab1552](https://doi.org/10.1093/mnras/stab1552)
- Chabrier, G. 2003, *Publications of the Astronomical Society of the Pacific*, 115, 763, doi: [10.1086/376392](https://doi.org/10.1086/376392)
- Cheng, T.-Y., Huertas-Company, M., Conselice, C. J., et al. 2021, *Monthly Notices of the Royal Astronomical Society*, 503, 4446, doi: [10.1093/mnras/stab734](https://doi.org/10.1093/mnras/stab734)
- Cheng, T.-Y., Conselice, C. J., Aragón-Salamanca, A., et al. 2020, *Monthly Notices of the Royal Astronomical Society*, 493, 4209, doi: [10.1093/mnras/staa501](https://doi.org/10.1093/mnras/staa501)
- Chiu, C.-C., Sainath, T. N., Wu, Y., et al. 2018, in 2018 IEEE International Conference on Acoustics, Speech and Signal Processing (ICASSP), 4774–4778, doi: [10.1109/ICASSP.2018.8462105](https://doi.org/10.1109/ICASSP.2018.8462105)
- Conselice, C. J. 2003, *The Astrophysical Journal Supplement Series*, 147, 1, doi: [10.1086/375001](https://doi.org/10.1086/375001)
- . 2014, *Annual Review of Astronomy and Astrophysics*, 52, 291, doi: [10.1146/annurev-astro-081913-040037](https://doi.org/10.1146/annurev-astro-081913-040037)
- Conselice, C. J., Bershad, M. A., & Jangren, A. 2000, *The Astrophysical Journal*, 529, 886, doi: [10.1086/308300](https://doi.org/10.1086/308300)
- Conselice, C. J., Rajgor, S., & Myers, R. 2008, *MNRAS*, 386, 909, doi: [10.1111/j.1365-2966.2008.13069.x](https://doi.org/10.1111/j.1365-2966.2008.13069.x)
- Dai, Y., Xu, J., Song, J., et al. 2023, *The Astrophysical Journal Supplement Series*
- Dark Energy Survey Collaboration, Abbott, T., Abdalla, F. B., et al. 2016, *MNRAS*, 460, 1270, doi: [10.1093/mnras/stw641](https://doi.org/10.1093/mnras/stw641)
- de Vaucouleurs, G. 1948, *Annales d'Astrophysique*, 11, 247
- Dieleman, S., Willett, K. W., & Dambre, J. 2015, *Monthly Notices of the Royal Astronomical Society*, 450, 1441, doi: [10.1093/mnras/stv632](https://doi.org/10.1093/mnras/stv632)
- Dimauro, P., Daddi, E., Shankar, F., et al. 2022, *Monthly Notices of the Royal Astronomical Society*, 513, 256, doi: [10.1093/mnras/stac884](https://doi.org/10.1093/mnras/stac884)
- Du, M., Ho, L. C., Debattista, V. P., et al. 2021, *The Astrophysical Journal*, 919, 135, doi: [10.3847/1538-4357/ac0e98](https://doi.org/10.3847/1538-4357/ac0e98)
- Euclid Collaboration, Scaramella, R., Amiaux, J., et al. 2022, *A&A*, 662, A112, doi: [10.1051/0004-6361/202141938](https://doi.org/10.1051/0004-6361/202141938)
- Fang, G., Ba, S., Gu, Y., et al. 2023, *The Astronomical Journal*, 165, 35, doi: [10.3847/1538-3881/aca1a6](https://doi.org/10.3847/1538-3881/aca1a6)
- Fielding, E., Nyirenda, C. N., & Vaccari, M. 2022, in 2022 International Conference on Electrical, 1, doi: [10.1109/ICECET55527.2022.9872611](https://doi.org/10.1109/ICECET55527.2022.9872611)
- Fisher, D. B., & Drory, N. 2008, *The Astronomical Journal*, 136, 773, doi: [10.1088/0004-6256/136/2/773](https://doi.org/10.1088/0004-6256/136/2/773)
- Freeman, K. C. 1970, *The Astrophysical Journal*, 160, 811, doi: [10.1086/150474](https://doi.org/10.1086/150474)
- Freeman, P. E., Izbicki, R., Lee, A. B., et al. 2013, *Monthly Notices of the Royal Astronomical Society*, 434, 282, doi: [10.1093/mnras/stt1016](https://doi.org/10.1093/mnras/stt1016)
- Gardner, J. P., Mather, J. C., Clampin, M., et al. 2006, *SSRv*, 123, 485, doi: [10.1007/s11214-006-8315-7](https://doi.org/10.1007/s11214-006-8315-7)
- Gauci, A., Zarb Adami, K., & Abela, J. 2010, arXiv e-prints, arXiv:1005.0390, doi: [10.48550/arXiv.1005.0390](https://doi.org/10.48550/arXiv.1005.0390)
- Ghosh, A., Urry, C. M., Wang, Z., et al. 2020, *ApJ*, 895, 112, doi: [10.3847/1538-4357/ab8a47](https://doi.org/10.3847/1538-4357/ab8a47)
- Grogin, N. A., Kocevski, D. D., Faber, S. M., et al. 2011, *ApJS*, 197, 35, doi: [10.1088/0067-0049/197/2/35](https://doi.org/10.1088/0067-0049/197/2/35)
- Gu, Y., Fang, G., Yuan, Q., Cai, Z., & Wang, T. 2018, *The Astrophysical Journal*, 855, 10, doi: [10.3847/1538-4357/aaad0b](https://doi.org/10.3847/1538-4357/aaad0b)
- Hartigan, J. A., & Wong, M. A. 1979, *Journal of the royal statistical society. series c (applied statistics)*, 28, 100
- Häußler, B., Vika, M., Bamford, S. P., et al. 2022, *Astronomy & Astrophysics*, 664, A92, doi: [10.1051/0004-6361/202142935](https://doi.org/10.1051/0004-6361/202142935)
- Hocking, A., Geach, J. E., Sun, Y., & Davey, N. 2018, *Monthly Notices of the Royal Astronomical Society*, 473, 1108, doi: [10.1093/mnras/stx2351](https://doi.org/10.1093/mnras/stx2351)
- Hubble, E. P. 1926, *The Astrophysical Journal*, 64, 321, doi: [10.1086/143018](https://doi.org/10.1086/143018)
- Huertas-Company, M., Rouan, D., Soucail, G., et al. 2007, *A&A*, 468, 937, doi: [10.1051/0004-6361:20066673](https://doi.org/10.1051/0004-6361:20066673)
- Huertas-Company, M., Mei, S., Shankar, F., et al. 2013, *MNRAS*, 428, 1715, doi: [10.1093/mnras/sts150](https://doi.org/10.1093/mnras/sts150)
- Ilbert, O., Arnouts, S., McCracken, H. J., et al. 2006, *Astronomy & Astrophysics*, 457, 841, doi: [10.1051/0004-6361:20065138](https://doi.org/10.1051/0004-6361:20065138)
- Ilbert, O., Capak, P., Salvato, M., et al. 2009, *The Astrophysical Journal*, 690, 1236, doi: [10.1088/0004-637X/690/2/1236](https://doi.org/10.1088/0004-637X/690/2/1236)
- Kartaltepe, J. S., Rose, C., Vanderhoof, B. N., et al. 2023, *The Astrophysical Journal Letters*, 946, L15, doi: [10.3847/2041-8213/acad01](https://doi.org/10.3847/2041-8213/acad01)
- Kauffmann, G., White, S. D. M., Heckman, T. M., et al. 2004, *Monthly Notices of the Royal Astronomical Society*, 353, 713, doi: [10.1111/j.1365-2966.2004.08117.x](https://doi.org/10.1111/j.1365-2966.2004.08117.x)
- Kawinwanichakij, L., Papovich, C., Quadri, R. F., et al. 2017, *The Astrophysical Journal*, 847, 134, doi: [10.3847/1538-4357/aa8b75](https://doi.org/10.3847/1538-4357/aa8b75)

- Koekemoer, A. M., Fruchter, A. S., Hook, R. N., & Hack, W. 2003, in *HST Calibration Workshop : Hubble after the Installation of the ACS and the NICMOS Cooling System*, 337
- Koekemoer, A. M., Aussel, H., Calzetti, D., et al. 2007, *The Astrophysical Journal Supplement Series*, 172, 196, doi: [10.1086/520086](https://doi.org/10.1086/520086)
- Laigle, C., McCracken, H. J., Ilbert, O., et al. 2016, *The Astrophysical Journal Supplement Series*, 224, 24, doi: [10.3847/0067-0049/224/2/24](https://doi.org/10.3847/0067-0049/224/2/24)
- Laureijs, R., Amiaux, J., Arduini, S., et al. 2011, arXiv e-prints, arXiv:1110.3193, doi: [10.48550/arXiv.1110.3193](https://doi.org/10.48550/arXiv.1110.3193)
- Law, D. R., Steidel, C. C., Erb, D. K., et al. 2007, *The Astrophysical Journal*, 656, 1, doi: [10.1086/510357](https://doi.org/10.1086/510357)
- Lehmann, E. L., & Casella, G. 2006, *Theory of point estimation* (Springer Science & Business Media)
- Li, Z., & Arora, S. 2019, arXiv e-prints, arXiv:1910.07454, doi: [10.48550/arXiv.1910.07454](https://doi.org/10.48550/arXiv.1910.07454)
- Lianou, S., Barmby, P., Mosenkov, A. A., Lehnert, M., & Karczewski, O. 2019, *Astronomy & Astrophysics*, 631, A38, doi: [10.1051/0004-6361/201834553](https://doi.org/10.1051/0004-6361/201834553)
- Lintott, C., Schawinski, K., Bamford, S., et al. 2011, *Monthly Notices of the Royal Astronomical Society*, 410, 166, doi: [10.1111/j.1365-2966.2010.17432.x](https://doi.org/10.1111/j.1365-2966.2010.17432.x)
- Liu, Y., Tu, H.-L., Zhou, C.-C., Liu, Y., & Zhang, F.-L. 2022, *Networks with Pixels Embedding: A Method to Improve Noise Resistance in Images Classification*, arXiv. <http://ascl.net/2005.11679>
- liu, Z., Zhang, F., Cheng, L., et al. 2023, arXiv e-prints, arXiv:2311.08995, doi: [10.48550/arXiv.2311.08995](https://doi.org/10.48550/arXiv.2311.08995)
- Lotz, J. M., Madau, P., Giavalisco, M., Primack, J., & Ferguson, H. C. 2006, *The Astrophysical Journal*, 636, 592, doi: [10.1086/497950](https://doi.org/10.1086/497950)
- Lotz, J. M., Primack, J., & Madau, P. 2004, *The Astronomical Journal*, 128, 163, doi: [10.1086/421849](https://doi.org/10.1086/421849)
- Lotz, J. M., Davis, M., Faber, S. M., et al. 2008, *The Astrophysical Journal*, 672, 177, doi: [10.1086/523659](https://doi.org/10.1086/523659)
- Martig, M., Bournaud, F., Teyssier, R., & Dekel, A. 2009, *The Astrophysical Journal*, 707, 250, doi: [10.1088/0004-637X/707/1/250](https://doi.org/10.1088/0004-637X/707/1/250)
- Martin, G., Kaviraj, S., Hocking, A., Read, S. C., & Geach, J. E. 2020, *MNRAS*, 491, 1408, doi: [10.1093/mnras/stz3006](https://doi.org/10.1093/mnras/stz3006)
- Masci, J., Meier, U., Cireşan, D., & Schmidhuber, J. 2011, in *Artificial Neural Networks and Machine Learning – ICANN 2011*, ed. T. Honkela, W. Duch, M. Girolami, & S. Kaski, Vol. 6791 (Berlin, Heidelberg: Springer Berlin Heidelberg), 52–59, doi: [10.1007/978-3-642-21735-7_7](https://doi.org/10.1007/978-3-642-21735-7_7)
- Massey, R., Stoughton, C., Leauthaud, A., et al. 2010, *Monthly Notices of the Royal Astronomical Society*, 401, 371, doi: [10.1111/j.1365-2966.2009.15638.x](https://doi.org/10.1111/j.1365-2966.2009.15638.x)
- Murtagh, F. 1983, *The Computer Journal*, 26, 354, doi: [10.1093/comjnl/26.4.354](https://doi.org/10.1093/comjnl/26.4.354)
- Murtagh, F., & Legendre, P. 2014, *Journal of Classification*, 31, 274, doi: [10.1007/s00357-014-9161-z](https://doi.org/10.1007/s00357-014-9161-z)
- Nazaré, T. S., da Costa, G. B. P., Contato, W. A., & Ponti, M. 2018, in *Progress in Pattern Recognition, Image Analysis, Computer Vision, and Applications*, ed. M. Mendoza & S. Velastín (Cham: Springer International Publishing), 416–424
- Omand, C. M. B., Balogh, M. L., & Poggianti, B. M. 2014, *Monthly Notices of the Royal Astronomical Society*, 440, 843, doi: [10.1093/mnras/stu331](https://doi.org/10.1093/mnras/stu331)
- Papovich, C., Giavalisco, M., Dickinson, M., Conselice, C. J., & Ferguson, H. C. 2003, *The Astrophysical Journal*, 598, 827, doi: [10.1086/378976](https://doi.org/10.1086/378976)
- Peng, C. Y., Ho, L. C., Impey, C. D., & Rix, H.-W. 2002, *The Astronomical Journal*, 124, 266, doi: [10.1086/340952](https://doi.org/10.1086/340952)
- Prevot, M. L., Lequeux, J., Maurice, E., Prevot, L., & Rocca-Volmerange, B. 1984, *Astronomy & Astrophysics*, 132, 389
- Ralph, N. O. 2019, *Publications of the Astronomical Society of the Pacific*, 17
- Rodriguez-Gomez, V., Snyder, G. F., Lotz, J. M., et al. 2019, *Monthly Notices of the Royal Astronomical Society*, 483, 4140, doi: [10.1093/mnras/sty3345](https://doi.org/10.1093/mnras/sty3345)
- Rosa, R. R., de Carvalho, R. R., Sautter, R. A., et al. 2018, *Monthly Notices of the Royal Astronomical Society: Letters*, 477, L101, doi: [10.1093/mnras/lsly054](https://doi.org/10.1093/mnras/lsly054)
- Scarlata, C., Carollo, C. M., Lilly, S., et al. 2007, *ApJS*, 172, 406, doi: [10.1086/516582](https://doi.org/10.1086/516582)
- Schawinski, K., Urry, C. M., Simmons, B. D., et al. 2014, *Monthly Notices of the Royal Astronomical Society*, 440, 889, doi: [10.1093/mnras/stu327](https://doi.org/10.1093/mnras/stu327)
- Schmidhuber, J. 2015, *Neural Networks*, 61, 85, doi: [10.1016/j.neunet.2014.09.003](https://doi.org/10.1016/j.neunet.2014.09.003)
- Schutter, A., & Shamir, L. 2015, *Astronomy and Computing*, 12, 60, doi: [10.1016/j.ascom.2015.05.002](https://doi.org/10.1016/j.ascom.2015.05.002)
- Scoville, N., Aussel, H., Brusa, M., et al. 2007, *The Astrophysical Journal Supplement Series*, 172, 1, doi: [10.1086/516585](https://doi.org/10.1086/516585)
- Sérsic, J. L. 1963, *Boletín de la Asociación Argentina de Astronomía La Plata Argentina*, 6, 41
- Simmons, B. D., Lintott, C., Willett, K. W., et al. 2017, *Monthly Notices of the Royal Astronomical Society*, 464, 4420, doi: [10.1093/mnras/stw2587](https://doi.org/10.1093/mnras/stw2587)
- Spergel, D., Gehrels, N., Baltay, C., et al. 2015, arXiv e-prints, arXiv:1503.03757, doi: [10.48550/arXiv.1503.03757](https://doi.org/10.48550/arXiv.1503.03757)
- Sreejith, S., Pereverzyev, Sergiy, J., Kelvin, L. S., et al. 2018, *MNRAS*, 474, 5232, doi: [10.1093/mnras/stx2976](https://doi.org/10.1093/mnras/stx2976)
- Szegedy, C., Liu, W., Jia, Y., et al. 2015, in *2015 IEEE Conference on Computer Vision and Pattern Recognition (CVPR)*, 1–9, doi: [10.1109/CVPR.2015.7298594](https://doi.org/10.1109/CVPR.2015.7298594)

- Tasca, L. A. M., Kneib, J. P., Iovino, A., et al. 2009, *A&A*, 503, 379, doi: [10.1051/0004-6361/200912213](https://doi.org/10.1051/0004-6361/200912213)
- Tohill, C. 2021, *The Astrophysical Journal*
- Treu, T., Calabrò, A., Castellano, M., et al. 2023, *The Astrophysical Journal Letters*, 942, L28, doi: [10.3847/2041-8213/ac9283](https://doi.org/10.3847/2041-8213/ac9283)
- van der Maaten, L., & Hinton, G. 2008, *Journal of Machine Learning Research*, 9, 2579
- Vega-Ferrero, J., Domínguez Sánchez, H., Bernardi, M., et al. 2021, *Monthly Notices of the Royal Astronomical Society*, 506, 1927, doi: [10.1093/mnras/stab594](https://doi.org/10.1093/mnras/stab594)
- Walmsley, M., Lintott, C., Géron, T., et al. 2021, *Monthly Notices of the Royal Astronomical Society*, 509, 3966, doi: [10.1093/mnras/stab2093](https://doi.org/10.1093/mnras/stab2093)
- Weaver, J. R., Kauffmann, O. B., Ilbert, O., et al. 2022, *The Astrophysical Journal Supplement Series*, 258, 11, doi: [10.3847/1538-4365/ac3078](https://doi.org/10.3847/1538-4365/ac3078)
- Willett, K. W., Galloway, M. A., Bamford, S. P., et al. 2017, *MNRAS*, 464, 4176, doi: [10.1093/mnras/stw2568](https://doi.org/10.1093/mnras/stw2568)
- Yao, X., Feng, X., Cheng, G., Han, J., & Guo, L. 2019, in 2019 IEEE International Geoscience and Remote Sensing Symposium, IGARSS 2019, Yokohama, Japan, July 28 - August 2, 2019 (IEEE), 1382–1385, doi: [10.1109/IGARSS.2019.8899285](https://doi.org/10.1109/IGARSS.2019.8899285)
- Yao, Y., Song, J., Kong, X., et al. 2023, *The Astrophysical Journal*, 954, 113, doi: [10.3847/1538-4357/ace7b5](https://doi.org/10.3847/1538-4357/ace7b5)
- York, D. G., Adelman, J., Anderson, John E., J., et al. 2000, *AJ*, 120, 1579, doi: [10.1086/301513](https://doi.org/10.1086/301513)
- Zhan, H. 2011, *Scientia Sinica Physica, Mechanica & Astronomica*, 41, 1441, doi: [10.1360/132011-961](https://doi.org/10.1360/132011-961)
- Zhan, H. 2018, in 42nd COSPAR Scientific Assembly, Vol. 42, E1.16–4–18
- Zhang, T., Ramakrishnan, R., & Livny, M. 1996, *ACM SIGMOD Record*, 25, 103, doi: [10.1145/235968.233324](https://doi.org/10.1145/235968.233324)
- Zhou, C., Gu, Y., Fang, G., & Lin, Z. 2022, *The Astronomical Journal*, 13
- Zhu, X.-P., Dai, J.-M., Bian, C.-J., et al. 2019, *Ap&SS*, 364, 55, doi: [10.1007/s10509-019-3540-1](https://doi.org/10.1007/s10509-019-3540-1)

Table 2. Part of The Final Catalogue

ID	R.A. (deg)	DEC. (deg)	I_{mag} mag	z	M_* ($\log M_{\odot}$)	r_e (kpc)	n	flag1	C	A	S	G	M_{20}	M	I	D	Ψ	G_2	flag2	Type
(1)	(2)	(3)	(4)	(5)	(6)	(7)	(8)	(9)	(10)	(11)	(12)	(13)	(14)	(15)	(16)	(17)	(18)	(19)	(20)	(21)
1	150.71249	1.79211	24.83	0.78	8.52	0.95	0.83	2	2.46	-0.17	0.03	0.46	-1.59	0.02	0.00	0.13	1.90	1.96	0	IRR
2	150.71818	1.79273	24.60	0.97	10.44	0.39	8.00	2	2.81	-0.01	0.00	0.48	-1.78	0.05	0.00	0.06	1.06	1.88	0	LTD
3	150.72869	2.54382	24.66	0.36	7.94	1.42	1.92	2	3.15	-0.14	-0.07	0.51	-1.63	0.27	0.40	0.28	2.38	1.79	0	LTD
4	149.63794	2.37729	24.06	0.89	9.09	3.14	0.20	2	1.89	-0.12	0.02	0.41	-0.83	0.24	0.76	0.29	8.60	1.78	0	IRR
5	150.71562	1.79362	21.31	0.39	9.66	4.36	0.72	2	2.70	0.01	0.03	0.46	-1.49	0.15	0.46	0.06	0.00	1.89	0	IRR
6	150.71684	1.79427	23.60	0.65	8.99	1.03	1.95	2	2.90	-0.12	0.02	0.48	-1.79	0.02	0.00	0.04	0.52	1.78	0	ETD
7	150.47448	2.33798	24.42	0.95	8.90	2.41	1.38	2	2.53	-0.35	0.02	0.38	-1.22	0.55	0.14	0.15	2.21	1.95	0	IRR
8	150.71614	1.79478	24.79	0.66	8.22	0.40	5.12	2	3.18	0.01	0.05	0.55	-1.75	0.04	0.00	0.09	1.12	1.78	0	LTD
9	150.49108	1.87574	22.54	0.45	9.80	1.81	8.00	2	3.53	0.05	0.00	0.59	-2.00	0.03	0.00	0.03	0.30	0.47	0	SPH
10	150.35723	2.29304	23.95	0.77	8.04	1.78	6.20	2	3.55	0.02	-0.02	0.60	-1.86	0.04	0.00	0.12	1.67	1.66	0	SPH
11	149.97418	1.70920	23.81	1.00	8.90	2.20	1.10	2	2.71	0.16	0.04	0.50	-1.34	0.23	0.27	0.19	3.65	1.81	0	LTD
12	150.71988	2.54496	24.19	0.66	8.70	0.82	0.87	2	2.46	0.08	0.05	0.50	-1.53	0.01	0.00	0.16	0.61	1.88	0	SPH
13	150.71874	2.54548	21.06	0.61	10.32	5.47	1.90	2	3.14	0.11	0.03	0.56	-1.94	0.02	0.10	0.03	0.00	0.93	0	ETD
14	150.49124	1.87773	23.29	0.96	9.66	2.76	1.29	2	2.73	0.09	0.01	0.45	-1.64	0.06	0.14	0.11	1.67	1.86	0	IRR
15	149.63540	2.37918	22.78	0.92	10.45	1.45	2.66	2	3.18	-0.01	0.01	0.55	-1.89	0.01	0.00	0.01	1.40	1.14	0	SPH
16	149.96909	1.70877	24.71	0.93	9.09	3.54	1.29	2	2.96	0.01	0.03	0.45	-1.55	0.16	0.36	0.20	6.72	1.84	0	IRR
17	150.72626	2.54642	22.00	0.36	9.39	1.67	1.50	2	3.02	0.07	0.02	0.53	-1.84	0.01	0.01	0.04	1.12	1.32	0	ETD
18	149.63316	2.37972	24.66	1.09	10.22	7.32	6.57	2	3.35	-0.09	0.03	0.48	-1.70	0.12	0.08	0.14	3.60	1.73	0	ETD
19	149.79397	2.37765	21.18	0.43	10.19	4.24	1.06	2	2.72	0.04	0.02	0.48	-1.77	0.02	0.10	0.04	nan	1.72	0	LTD
20	150.72653	1.79572	22.05	0.82	9.34	2.95	4.35	2	3.91	0.24	0.02	0.57	-1.88	0.42	0.17	0.02	3.53	0.86	0	SPH

NOTE—(1) Sequential number identifier; (2) R.A. expressed in decimal degrees; (3) decl. expressed in decimal degrees; (4), (5), and (6) are magnitude in I band, redshift, and stellar mass from Weaver et al. (2022), respectively; (7) effective radius; (8) Sérsic index; (9) flag of single Sérsic fitting, 2 represents a good fitting; (10), (11), (12), (13), (14), (15), (16), (17), (18), and (19) represent C, A, S, Gini, M_{20} , M, I, D, Ψ , and G_2 coefficient, respectively, (20) flag of the nonparametric morphological measurements, 0 represents a good measurement; (21) galaxy morphological type.